An experimental investigation of the behaviour of steels over large temperature and strain rate ranges

Anis Hor*, Franck Morel, Jean-Lou Lebrun, Guénaël Germain

Arts et Métiers ParisTech, CER Angers - Laboratoire LAMPA, 2 Bd du Ronceray, 49035 Angers, Cedex 1, France

Keywords:
Rheology
Compression tests
Shear tests
42CrMo4 steel
100Cr6 steel
Processing maps

A B S T R A C T

During forging and machining manufacturing processes, the material is subject to large strains at high strain rates which provoke local heating and microstructural changes. Modelling of these phenomena requires precise knowledge of the stress–strain constitutive equations for a large range of strains, strain rates and temperatures. An experimental study of the rheology of both hyper- and hypo-eutectoid steels (with different microstructures) over a temperature range from 20 °C to 1000 °C and with strain rates from 10^{-2} to 10^{5} s^{-1} has been undertaken. These tests were performed in compression on cylindrical specimens and in shear using hat-shaped specimens. Both a GLEEBLE 3500 thermomechanical testing machine and a Split-Hopkinson Pressure Bar apparatus were used. From these tests, three *deformation domains* have been identified as a function of the material behaviour and of the changes in the deformed microstructure. Each domain was characterized by its behaviour, including the competition between hardening and softening, strain rate sensitivity on the flow stress and the softening phenomenon (i.e. recrystallisation or recovery, etc.). Finally, based on thermodynamical considerations, the conditions of thermoplastic instability (i.e. shear bands, twinning, heterogeneities, etc.) and microstructural changes are highlighted using process maps of the dissipated power repartition.

1. Introduction

Recent work on thermomechanical manufacturing processes such as machining and forging is often based on simulation tools like the finite element method and is done with the aim of predicting the forming process. It can be noted that this work is often focused exclusively on the numerical problems related to the use of the finite element method in this context or the investigation of problems such as material separation, frictional contact, very large deformation, etc. Due to advances in these areas, the simulation of these manufacturing processes is more easily undertaken. However, other factors, such as frictional behaviour and stress–strain constitutive equations become the limiting factors in terms of undertaking accurate numerical simulations. Determining the stress–strain constitutive equations and the associated material parameters is extremely difficult due to the extreme character of the loads to which the material is subject during machining and/or forging operations.

The study of the thermomechanical loads seen by a material during forming has been the object of several investigations. For example, Changeux and Lebrun [1] showed that during machining, the strain can attain values close to 5. MSaoubi et al. [2] estimated that during machining of steels, the temperature in the secondary shear zone can be up to 800 °C. Calamaz et al. [3] showed that the loading mode in machining results in a combination of shear stress and compressive stress. Finally, Montheillet [4] placed the different manufacturing processes in a strain rate versus temperature diagram. He showed that during forging and machining, the material is submitted to strains with a strain rate ranging from 10^{-2} to 10^{5} s^{-1} (see Fig. 1).

Therefore, experimental rheology studies during machining and forging require the use of tests that cover the complete strain rate range, going from the quasi-static to the dynamic range and the complete temperature range, going from ambient temperature to temperatures close to the melting temperature of the material. However, very little work has been published concerning the determination of the material parameters necessary to identify the stress–strain constitutive equations for the manufacturing processes modelling. The available studies are based on experimental data which is often very limited. In general a minimum number of tests are done in order to identify the chosen constitutive model without comparing its domain of validity with the loads applied to the material during machining [5] or forging [6].

Studies considering the experimental behaviour over a large strain rate range and temperature range are rare. Based on data from the literature, Lurdos [7] regrouped the experimental test conditions concerning the 316L stainless steel. He showed that much data is missing in the zone corresponding to semi-hot

* Corresponding author. Tel.: +33 241207336; fax: +33 241207320.
E-mail addresses: anis.hor@ensam.eu, hor.anis@yahoo.fr (A. Hor).

http://dx.doi.org/10.1016/j.ijmecsci.2013.01.003

deformation (i.e. $0.3 \le T/T_f \le 0.5$) and there is a complete absence of data in the hot dynamic domain (i.e. domain 4 in Fig. 1).

Processing maps offer a way of analysing the constitutional behaviour of a material due to deformation. This approach can be used to highlight microstructural changes that occur during deformation. It is based on the evaluation of the complementary dissipated power (J) using the relation between strain rate ($\dot{\varepsilon}$) and flow stress (σ) during the deformation process. The experimental data presented in this work are analysed using this methodology.

Based on thermodynamical considerations, Prasad et al. [8,9] proposed that the optimal thermomechanical conditions for deformation correspond to the maximum value of J. Indeed, Ziegler [10] has shown that the behaviour of the deformation process follows the principle of the maximum entropy production rate, which is equivalent to the principal of the minimum force or the minimum irreversible strain rate in a force or strain rate space.

At a given temperature, the rate of the dissipated work is directly proportional to the internal entropy production rate, which, based on the irreversibility principle, is always positive:

$$P = \sigma\,\dot{\varepsilon} = T\frac{dS}{dt} \ge 0, \tag{1}$$

where σ is the effective stress, $\dot{\varepsilon}$ is the effective strain rate, T is the temperature and dS/dt is the internal entropy production rate. The total entropy production rate is composed of two complementary parts. The first part, which is generally larger, is the *conduction entropy* which is due to heat conduction from the plastically deformed region to the colder regions of the specimen.

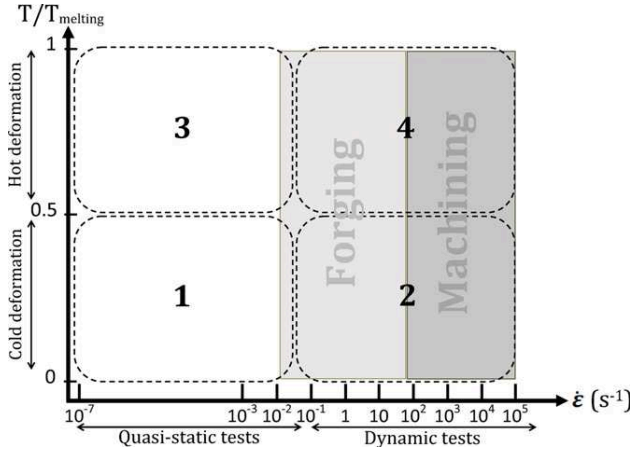

Fig. 1. Imposed strain rate (in s^{-1}) and temperature ranges in forging and machining operations and different domains of mechanical behaviour.

The second part is due to the microstructural dissipation which reduces the flow stress required for plastic deformation. Ziegler [10] represented both contributions in terms of dissipative functions in the strain rate and force space, and showed that the instantaneous total power dissipated $(\sigma,\dot{\varepsilon})$ is given by

$$P = \int_0^{\dot{\varepsilon}} \sigma\, d\dot{\varepsilon} + \int_0^{\sigma} \dot{\varepsilon}\, d\sigma = G + J. \tag{2}$$

The first integral is the content dissipated power G, the second is the co-content or the complementary dissipated power J (see Fig. 2(a)). The shape of the $\sigma = f(\dot{\varepsilon})$ curve gives an indication of the part of the dissipated power that is used for heat conduction and the part used for microstructural dissipation. Viscoplasticity is caused by this dissipation due to the microstructure.

A power law is often used to describe the relationship $\sigma = f(\dot{\varepsilon})$ for plastic deformation:

$$\sigma = K(T,\varepsilon,\dot{\varepsilon})\dot{\varepsilon}^{m(T,\varepsilon,\dot{\varepsilon})}. \tag{3}$$

For fixed values of T and ε, it is possible to examine the quantities $(\Delta J/\Delta G)$ and $(\Delta J/\Delta P)$ for small variations of $\dot{\varepsilon}$ in order to obtain an indication of the change in dissipation mechanism. By assuming that the dependence of K and m on the strain rate $\dot{\varepsilon}$ is small, the instantaneous values of ΔJ, ΔG and ΔP are given by the integrals:

$$\begin{aligned} \Delta J &\approx \int_{\sigma}^{\sigma+\Delta\sigma} \dot{\varepsilon}\, d\sigma \\ \Delta G &\approx \int_{\dot{\varepsilon}_0}^{\dot{\varepsilon}_0+\Delta\dot{\varepsilon}_0} \sigma\, d\dot{\varepsilon} \\ \Delta P &\approx K(\dot{\varepsilon}+\Delta\dot{\varepsilon})^{m+1}. \end{aligned} \tag{4}$$

Prasad [8] defined the efficiency of the power dissipation (η) by a linear dissipater $(m=1)$ so that

$$\frac{\Delta J/\Delta P}{(\Delta J/\Delta P)_{lineaire}} = \frac{m/(m+1)}{1/2} = \frac{2m}{m+1} \equiv \eta. \tag{5}$$

This highlights the importance of the parameter m, which defines the relative importance of the division of the power between heat production and microstructural change. The value of m is between 0 and 1 for stable flow of a viscoplastic solid [10]. An increase in m results in an increase in microstructural dissipation. A negative value of m (commonly referred to negative strain rate sensitivity) is observed for dynamic ageing, where mobile dislocations are repeatedly locked and unlocked by the speed at which solute atoms are moved. In terms of solid mechanics, when $m > 1$ the term *locking solids* is discussed [11]. These two extremes represent unstable flow.

In this context, the present work consists of a complete experimental investigation of three steels: (a) 42CrMo4 with a

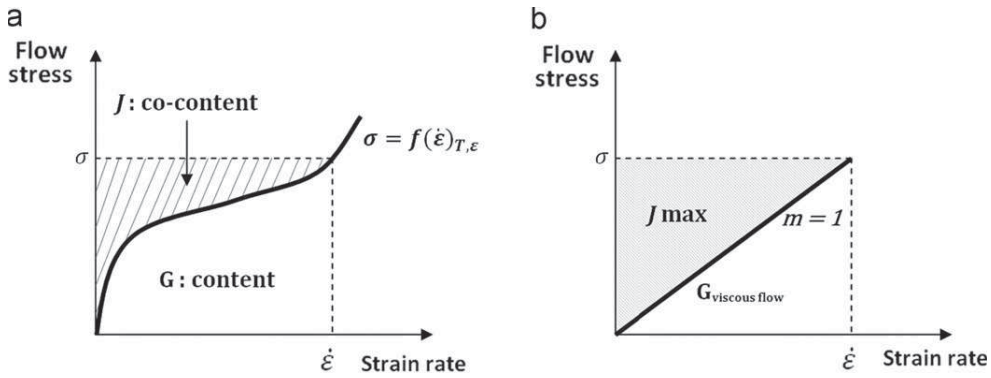

Fig. 2. Schematic representation of (a) the content (G) and co-content (J) dissipated power for a material with a behaviour given by a curve $\sigma = f(\dot{\varepsilon})$ (the total dissipated power is given by the rectangle) and (b) the maximum complementary dissipated power J_{max} obtained for a sensitivity to the strain rate $m=1$ [9].

ferrito-perlitic microstructure, (b) 42CrMo4 with a bainitic microstructure and (c) 100Cr6 in the annealed state. The compressive and shear loading modes are studied. The experimental campaign makes it possible to detect all of the macro and microscopic physical phenomena involved in the deformation process and to analyse the temperature and strain rate sensitivity of the materials investigated over a wide range of rheological parameters.

2. Materials and methods

2.1. Materials

This work is focused on two steels often used in machining and forging operations:

- The 42CrMo4 steel (AISI 4140) is a low alloy hypo-eutectoid steel ($\%\,C < 0.85$) with chromium and molybdenum as main alloying elements. This steel is studied in two initial microstructural states. The first is the steel with an initial ferrito-perlitic microstructure is referred to as 42*CrMo4-FP*. The microstructure is composed of grains of ferritic and pearlitic (see Fig. 3(a)). The hardness is 248 HB. The second is the steel with an initial bainitic microstructure (see Fig. 3(b)) is referred to as 42*CrMo4-BA*. This material is harder (approximately 310 HB) than the ferrito-perlitic version. The chemical composition is very similar to that measured for the ferrito-perlitic microstructure.
- The 100Cr6 steel (AISI 52100) is a hyper-eutectoid, low chromium, steel ($\%\,C > 0.85$). The chemical composition of this steel, determined by spark emission spectroscopy is given in Table 1. This steel is principally used for the manufacture of ring and ball bearings. Bars of the 100Cr6 material were used in the annealed state. Its microstructure consists of carbides dispersed in a ferritic matrix with a low carbon content (see Fig. 3(c)). The hardness is 272 HB. In the following this material will be referred to as 100*Cr6-FP*.

2.2. Experimental tools

In order to test the materials at temperatures ranging from ambient temperature to hot-forging temperatures and to cover the range of strain rates going from 10^{-2} to $10^{4}\ s^{-1}$, two different experimental set-ups were used:

- A GLEEBLE 3500 thermomechanical testing machine: the temperature measurement and control was done using a thermocouple welded to the specimen. The specimen was tested in a primary vacuum chamber. Mechanically, the GLEEBLE can achieve displacement speeds of 10^{-4} to $2\ m\ s^{-1}$. The measurement and strain control was done using a quartz longitudinal extensometer placed on the jaws. Depending on the desired speed, two configurations can be used. For low speeds, the normal configuration was used, involving a hydraulic actuator capable of applying a compressive force to the specimen (see Fig. 4). For high speeds ($> 10^{-2}\ m\ s^{-1}$) the hydraulic ram was decoupled in order to accelerate before hitting the specimen. This configuration results in a shock at the moment of impact between the two parts of the decoupled actuator.
- Split Hopkinson Pressure Bar (SHPB) apparatus: this technique based on elastic wave transmission between the bars and the specimen was largely used for dynamic tests. The apparatus used allows strain rates of the order of $10^{3}\ s^{-1}$ in compression test. The projectile velocity can reach $25\ m\ s^{-1}$. However, it was not equipped with a heating system, therefore only tests at ambient temperature can be done.

2.3. Experimental tests

Two types of tests are analysed in this study: compression test and shear test on hat-shaped specimens.

The compression test specimens had a cylindrical shape with an initial diameter of $\varnothing 8$ mm and an initial length of 12 mm. The applied thermal cycle is illustrated in Fig. 5(a): it consists of heating the material at a constant heating rate of 5 °C/s up to the test temperature. The temperature is then held constant for 20 s to homogenize and stabilize the temperature along the specimen without desoldering thermocouples. Then the material is deformed at a constant strain rate. Finally, heating is stopped and the specimen is cooled in vacuum. Each point in Fig. 5(b) corresponds to a test condition for which three or more tests have

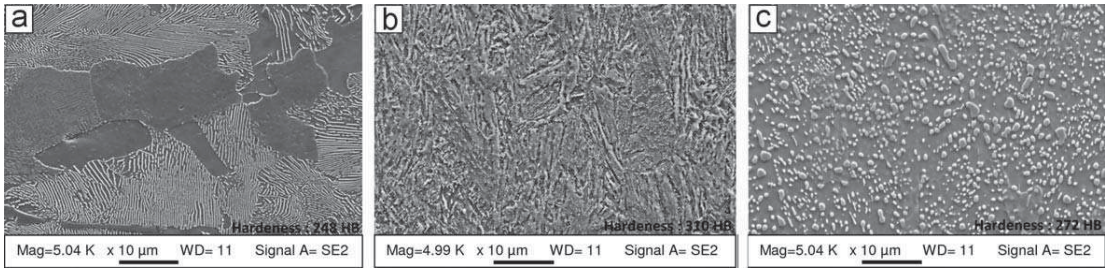

Fig. 3. The initial microstructures of the three steels studied: (a) 42CrMo4-FP, (b) 42CrMo4-BA and (c) 100Cr6-FP.

Table 1
Chemical composition of the three steels studied.

Element	C	Cr	Mn	Si	Cu	Ni	Mo	S
42CrMo4-FP (wt%)	0.40	1.10	0.85	0.23	0.24	0.10	0.20	0.06
42CrMo4-BA (wt%)	0.43	1.16	0.72	0.175	0.2	0.21	0.17	0.04
100Cr6-FP (wt%)	1.03	1.41	0.33	0.24	0.14	0.13	0.02	0.01

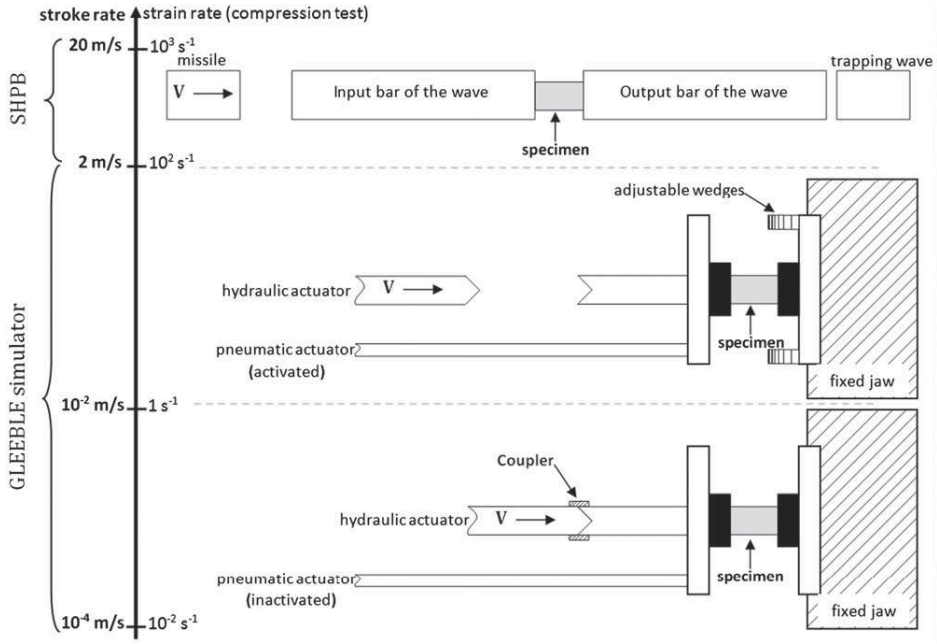

Fig. 4. The three configurations used for compression (and shear) tests done using a GLEEBLE machine and a Split Hopkinson Pressure Bars apparatus.

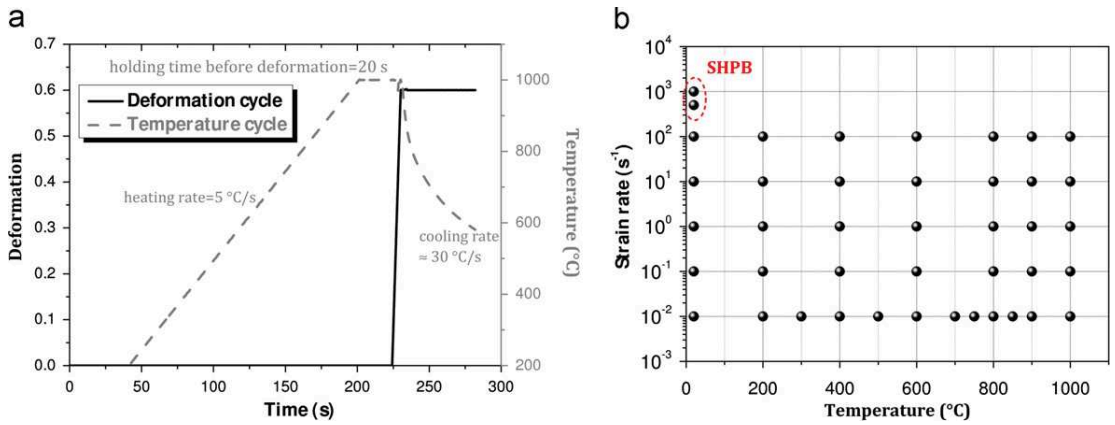

Fig. 5. (a) Applied thermal–mechanical cycle, (b) the different test conditions are investigated.

been conducted, to ensure repeatability. Additional tests were done if deemed necessary.

The elastic strain was deleted, taking into account the stiffness of the machine and the anvils. For high strain rate and high temperature tests, the measured force–displacement curves were smoothed in order to reduce the effect of the shock and the thermal effects caused by the temperature regulation (i.e. the effect of the control system). Precautions were taken to ensure that the temperature and strain distribution within the specimens were uniform. The latter was judged uniform up to a value of 0.5 [12]. Experimental techniques were also used to reduce the effects of friction (i.e. hot anvils, graphite sheets and nickel paste). The final shape of the specimens were verified to ensure that they remained globally cylindrical. The plastic strain is $\varepsilon^p = \varepsilon - \sigma/E(T)$ where $E(T)$ is Young's modulus taking into account the machine stiffness evolution with temperature [12,13], and ε is the positive true strain. Finally, for tests at high speeds ($\dot{\varepsilon}$ greater than 1 s^{-1}), since the strain rate is not uniform, average strain determined by $\dot{\varepsilon} = \varepsilon_f/\Delta t$, where ε_f is the total deformation and Δt is the total test time. The instantaneous and the average strain rates were almost identical, except at the start of the test.

Furthermore, the compression tests described above highlighted the existence of several physical and microstructural changes in the tested steels. These phenomena are however affected by the loading mode. Moreover, the strain (up to 0.5) and the strain rate (up to 10^3 s^{-1}) are lower than those encountered during machining for which macroscopic strain localization in the form of shear bands is often observed. Compression tests are generally homogeneous and cannot reproduce this type of localization. For these reasons, shear tests have been conducted on specimens referred to as "hat-shaped specimens". They are often used to characterize the formation of adiabatic shear bands [14,15] and to identify constitutive equations for the machining simulation [1,16].

The experimental set-up in the GLEEBLE testing machine and the Hopkinson bars are identical to those used for the compression tests, only the geometry of the specimen is different. The compression of this geometry results in a shear zone (see Fig. 6). It starts at the fillet radius (between the two cylinders) and propagates towards the centre. The resulting shear produces a plastic instability (in particular for dynamic tests) close to that observed in the primary shear zone in machining. This shear zone

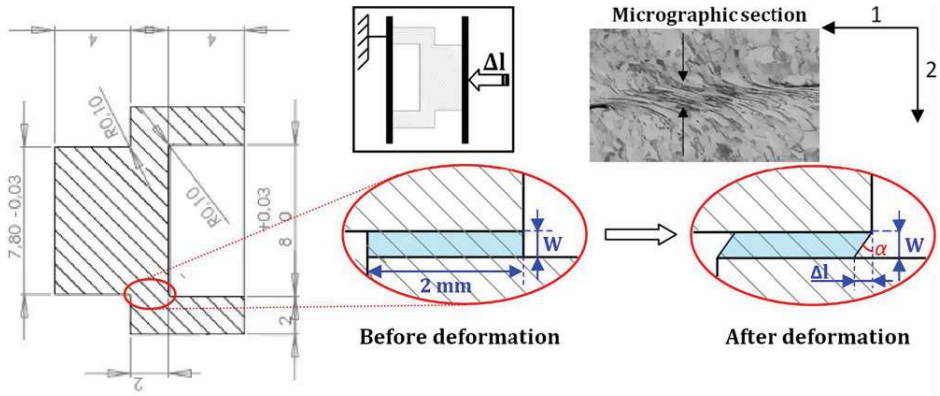

Fig. 6. Theoretical shear zone.

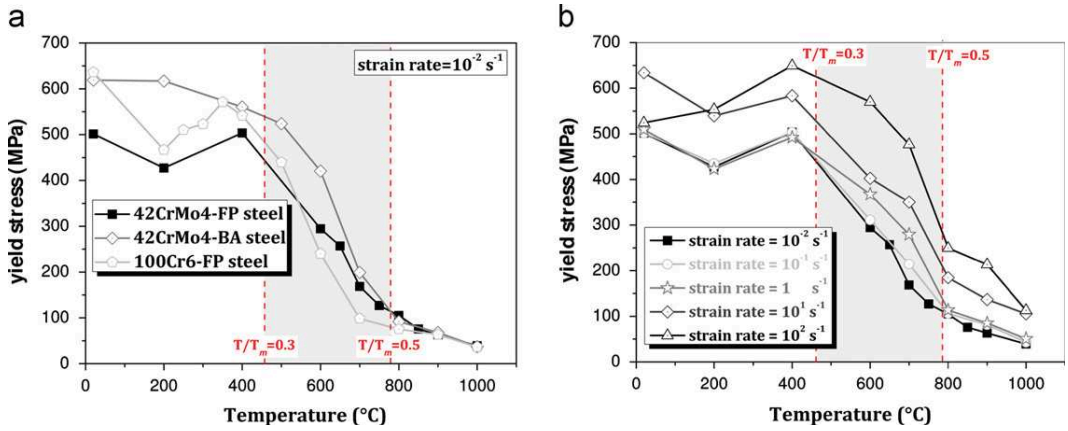

Fig. 7. Evolution of the compressive yield stress as a function of the temperature (a) for the three steels investigated, and (b) for the 42CrMo4-FP steel, at different strain rates.

is of very small width (0.1 mm max) which results in a higher equivalent strain rate, compared to the compression tests, with the same displacement rate. For example, for a displacement rate of 1 ms^{-1}, an equivalent strain rate of 10^4 s^{-1} can be obtained in shear, compared to 10^2 s^{-1} in compression. By using the parameters shown in Fig. 6, the theoretical shear stress and strain are determined experimentally:

$$\tau_{theo} = \frac{F}{\pi h\left(\frac{d_i + d_e}{2}\right)} \quad \text{and} \quad \gamma_{theo} = \tan\alpha = \frac{\Delta l}{W}, \tag{6}$$

where d_i and d_e are the interior diameter of the hollow part and the exterior diameter of the solid part of the specimen, respectively. $h=2$ mm is the length of the shear zone, $W = d_i - d_e/2 =$ 0.1 mm is the theoretical width of this zone and Δl is the displacement measured by a longitudinal extensometer.

This calculation assumes that $W=0.1$ mm is the width of the shear zone. Several authors [1,15] have shown that it can vary depending on the imposed thermomechanical cycle (rate and temperature) and the material studied. In this work, the theoretical shear stress and strain have been verified using finite element calculations with the Johnson–Cook constitutive equation [17] identified for the 42CrMo4-BA steel. The theoretical values were very similar to the numerical ones, regardless of the thermomechanical conditions [12].

The experimental results are presented in the $(\tau_{theo}, \gamma^p_{theo})$ space. The equivalent strain rate is determined from the shear rate by $\dot{\varepsilon} = \dot{\gamma}_{theo}/\sqrt{3}$. A large number of tests have been conducted on two materials: the 42CrMo4-BA steel and the 100Cr6-FP steel. The repeatability of these tests is generally low because of the complex specimen geometry especially at the inner and outer fillet radii which determines the shear zone (see Fig. 6). Each test condition is repeated several times until at least three similar curves are obtained, the dimensions of each specimen being verified before testing.

3. Results

3.1. Global behaviour

The 0.2% offset yield stress has been determined from the experimental stress–strain curves in compression. The evolution of this parameter as a function of the temperature shows a change in slope when passing from one deformation domain to another for the three steels investigated (see Fig. 7(a)). For the cold deformation domain ($T/T_f < 0.3$), the influence of temperature on the yield strength is small. However, during semi-hot deformation (i.e. $0.3 \le T/T_f \le 0.5$) this material parameter becomes very sensitive to the temperature. Finally, in the hot deformation range (i.e. $T/T_f > 0.5$) the yield strength is very low and is almost independent of temperature.

In order to analyse the strain rate sensitivity on the compressive yield stress, the temperature dependence of compressive yield stress of the 42CrMo4-FP steel is compared for different strain rates (see Fig. 7(b)). Fig. 7(b) shows that for strain rates between 10^{-2} and 1 s^{-1}, the curves are almost identical. For all temperatures, an increase in the yield stress was observed for

strain rates greater than 10 s^{-1}. This could be thought of as the limit between a quasi-static behaviour, where the yield stress is effectively independent of the strain rate, and a dynamic behaviour. The temperature sensitivity on the yield stress was not affected by the strain rate. This simple analysis of the sensitivity of the compressive yield stress on two rheological parameters (i.e. temperature and strain rate) highlights the different types of behaviour of the three steels studied. That is, cold, semi-hot and hot deformation, in terms of temperature and quasi-static and dynamic behaviour, in terms of strain rate.

In the following, the material behaviour will be analysed for both loading cases (compression and shear) in terms of strain rate and temperature sensitivity on the flow stress. The results for the compression tests are given in Figs. 8 and 9 for the shear tests.

From Fig. 8, it can be seen that for a given strain rate (10^{-2} s^{-1}) an elevation of temperature translated the stress–plastic strain curves towards the bottom, for all three steels. A radical change could be observed in the shape of these curves. The slope of the curves can be both positive indicating work hardening and negative indicating softening. Therefore, as well as causing a decrease in the flow stress, the temperature often plays a role in softening the material. With respect to this competition between work hardening and softening, three deformation domains can be distinguished, as a function of the temperature.

The conclusions made based on the compression tests remain valid for the shear loading mode, in particular the existence of three deformation domains and similar temperature sensitivity on the flow stress (Fig. 9). Although the attained shear levels were

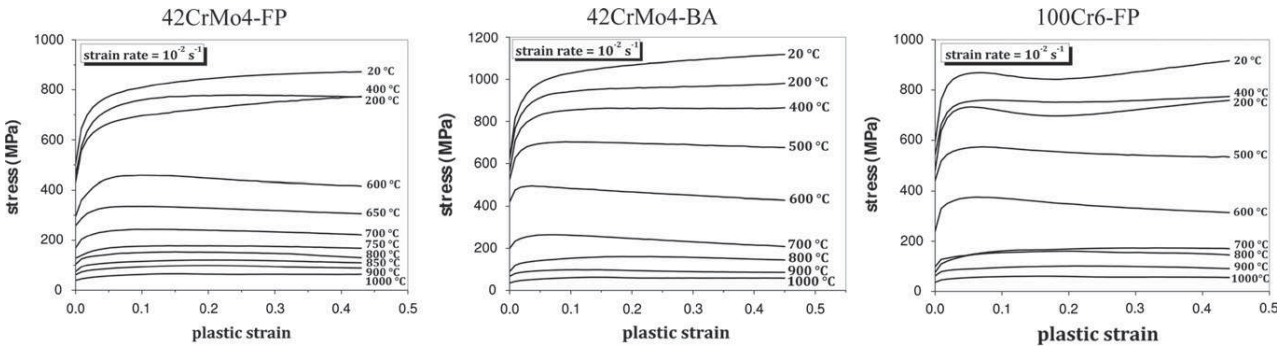

Fig. 8. Evolution of the compressive stress as a function of plastic strain for the three steels investigated at different temperatures and at a strain rate of 10^{-2} s^{-1}.

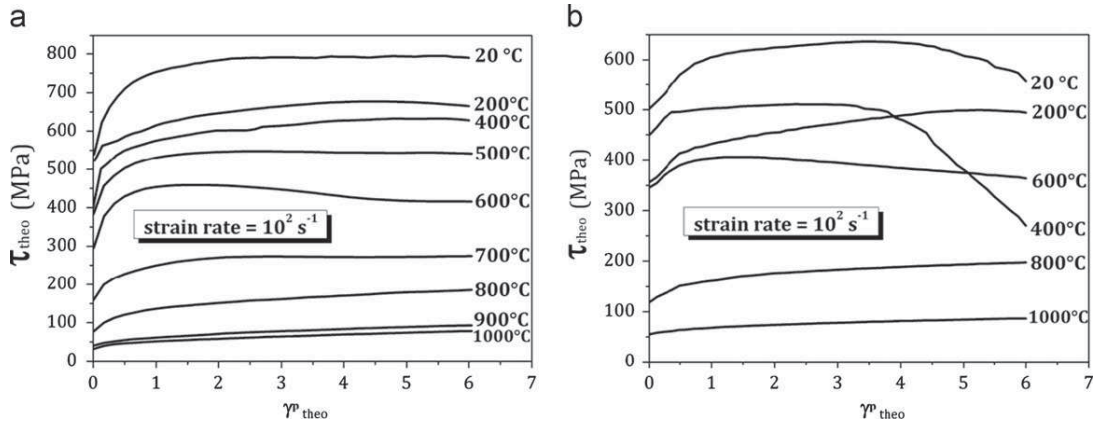

Fig. 9. Evolution of the shear stress as a function of the plastic shear strain for (a) the 42CrMo4-BA steel and (B) the 100Cr6-FP steel, at different temperatures and an equivalent strain rate of 10^2 s^{-1}.

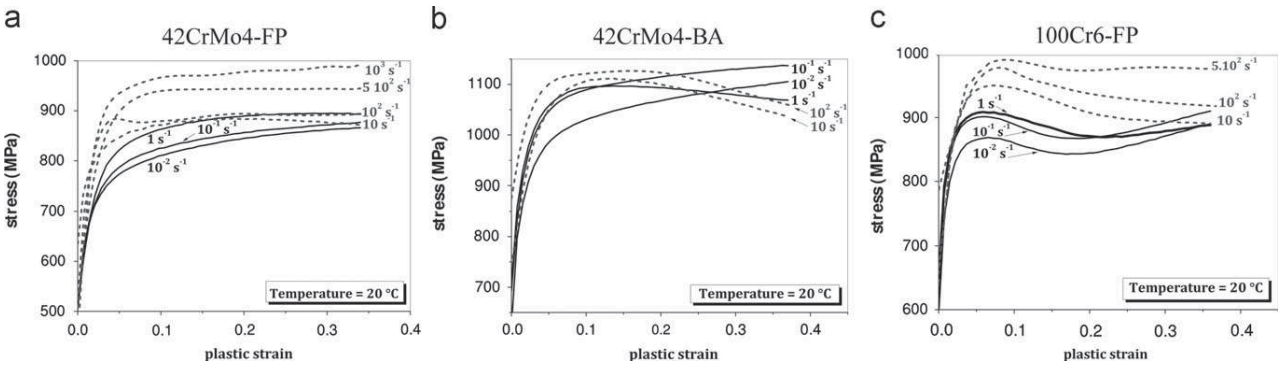

Fig. 10. Evolution of the compressive stress as a function of the plastic strain at 20 °C for different strain rates. Comparison between the three steels studied.

very high (6), the saturation stress was observed only for certain temperatures and equivalent strain rates. The equivalent strain rate sensitivity on the flow stress is temperature dependent. This sensitivity is analysed in the following for the three domains. The phenomenon between 200 and 400 °C observed for the two loading conditions (compression and shear) for the ferrito-pearlitic steels will be discussed later (see Section 3.3 and Fig. 25).

3.1.1. Cold deformation domain ($T/T_f < 0.3$)

In this domain, work hardening is the phenomenon observed at low strain rate, for the three steels studied. An increase in strain rate results in a slight increase in the stress level. The strain rate sensitivity on the stress is practically negligible in this strain rate interval (between 10^{-2} and $10^{2}\ s^{-1}$). However, the strain rate plays a role in terms of softening. The greater the strain rate, the lower the hardening. It even becomes negative for the 42CrMo4-BA steel and the 100Cr6-FP (see Fig. 10). The softening phenomenon is a function of the strain rate in this deformation domain. Softening caused by an increase in the strain rate can appear after a change in the deformation mechanism caused by the speed of the deformation process. It can also be caused by adiabatic heating effect. Indeed, during dynamic test, the plastic power is converted into heat which cannot be evacuated for this range of strain rate. We call this phenomenon *self-heating*. Note that softening also depends on the microstructure of the material. It is more intense for the 100Cr6-FP and the 42CrMo4-BA steels. At a strain rate of approximately $10\ s^{-1}$ (depending on the material), the flow curves are of adiabatic nature. The plastic power conversion is responsible for heating the specimen and decreasing the flow strength. The flow stress of dynamic flow curves can be lower than the quasi-static curves after severe deformation. The fact that the heat conductivity of an austenitic structure is lower than that of a ferritic structure should also be taken into consideration.

To evaluate the level of self-heating, the evolution of the temperature was measured during a test in which the initial temperature was 20 °C and with a strain rate of $\dot{\varepsilon} = 10^{2}\ s^{-1}$. Fig. 11 shows than an increase in the surface temperature of approximately 120 °C was measured during the test. It is very likely that the temperature in the centre of the specimen was higher. This is reinforced by the observed time difference between the rapid compression of the specimen and the appearance of a high surface temperature. A non-negligible period of time was necessary for the surface temperature to increase. A large part of this heat was also dissipated via conduction to the anvils used to compress the specimen or by radiation. This is consistent with the behaviour curves where softening occurs in the final part of the deformation. This phenomenon caused that the flow stress to be lower with respect to the quasi-static tests [18]. In the literature, constitutive models are typically based on isothermal flow curves. Consequently adiabatic flow curves should be corrected to isothermal flow curves. The dependency of adiabatic heating should be included in the constitutive equations [19]. Self-heating is therefore a phenomenon that provokes a softening effect and reduces the level of work hardening for steel materials. However, it cannot be the only factor responsible for the softening phenomenon, given the comparison between the temperature sensitivity of the steel and the self-heating temperature (see Fig. 11(a)).

To quantify the influence of self-heating on the stress–strain curves for the 42CrMo4-BA steel, two axisymmetric finite element simulations were carried out. The first one assumes that the flow is isothermal and the second assumes adiabatic flow where the conversion coefficient of the plastic power into heat (Taylor–Quinney factor) is equal to 0.95. The Abaqus Explicit finite element code was used in conjunction with a Johnson–Cook constitutive equation [17]. The material parameters were identified in [12]. Frictional effects were neglected in both cases. The conditions corresponding to a maximum increase in temperature (i.e. for a mean strain rate of $10^{2}\ s^{-1}$ and a temperature of 20 °C) were chosen for investigation. This is because increasing the temperature or decreasing the strain rate results in a decrease of the plastic power and therefore causes the self-heating temperature to drop. For the adiabatic flow model, the temperature at the node corresponding to the thermocouples location is of the order of 135 °C for a mean strain of 0.5 (see Fig. 11(b)). This result is almost identical to the experimental measurements obtained under the same conditions, but for the 42CrMo4-FP steel. Locally the temperature is higher. Fig. 12 shows that, at the center of the specimen, the temperature can reach upto 180 °C (453 K).

Finally the comparison between the isothermal and adiabatic flow curves and the experimental curve for an extreme case (20 °C and $\dot{\varepsilon} = 10^{2}\ s^{-1}$) shows the phenomenon of softening due to the self-heating temperature increase for the experimental case and the adiabatic flow calculation (see Fig. 13). The trend was reversed when self-heating was neglected and the slope of the stress–strain curve became positive. However, the relative differences between the three curves remained low (below 7%) up to a strain of 0.4. The low conductivity of steel and the tests conducted with high strain rates definitely assist in absorbing a great deal of this error. The study of thermoplastic stability was made for a range of strain rates between 10^{-2} and $10^{2}\ s^{-1}$. Therefore, the effect of self-heating on the flow stress were neglected and the stress levels used to determine the processing maps corresponded to the levels obtained experimentally.

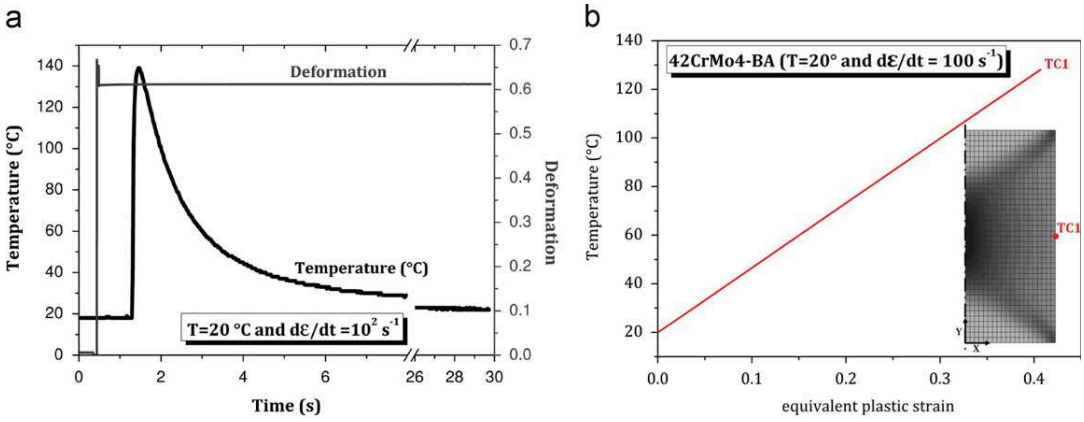

Fig. 11. Increase of the temperature during deformation due to self-heating for a compression test at $T = 20$ °C and $\dot{\varepsilon} = 10^{2}\ s^{-1}$. Comparison between (a) the experimental measurement the 42CrMo4-FP steel and (b) the FE prediction for the 42CrMo4-BA steel.

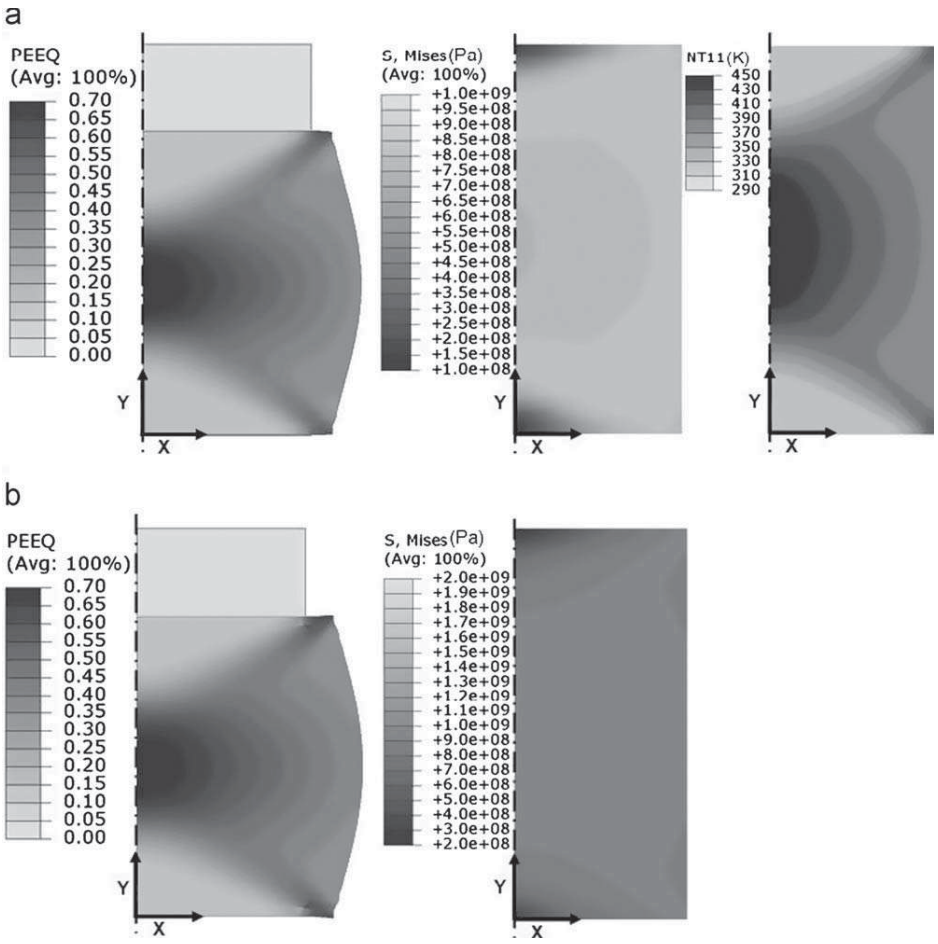

Fig. 12. Comparison between equivalent strain, temperature and equivalent stress maps obtained by FE calculation with Abaqus Explicit for (a) adiabatic flow and (b) isothermal flow.

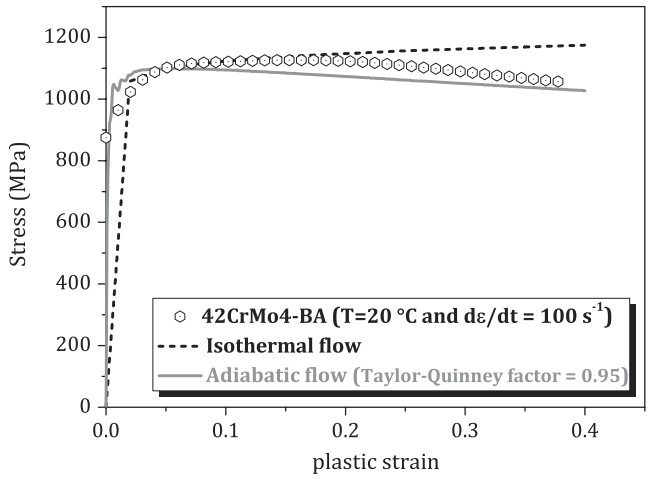

Fig. 13. Comparison between the stress–strain curves for the case of adiabatic flow (with a Taylor–Quinney factor = 0.95) and isothermal flow for the 42CrMo4-BA steel at $T = 20\ ^{\circ}\mathrm{C}$ and $\dot{\varepsilon} = 10^2\ \mathrm{s}^{-1}$.

For the shear tests, the stress increased with the equivalent strain rate. For equivalent strain rates between 10^{-1} and $10^3\ \mathrm{s}^{-1}$, the increase was modest. From $10^3\ \mathrm{s}^{-1}$, the rate sensitivity became important and the shape of the curves also changed for both steels (see Fig. 14). These observations are consistent with the phenomena observed during compression tests. For the three materials studied, the strain rate sensitivity on the flow stress was low in the cold deformation domain. However, the strain rate range studied in the compression tests did not allow the observation of fast dynamic behaviour.

Concerning the shape of the quasi-static curves, the flow stress increased to a saturation state for strains of the order of 1.5. Beyond this value, the curves stabilized until the appearance of macroscopic damage (which was removed during the treatment of the curves). From the equivalent strain rate of $10^3\ \mathrm{s}^{-1}$, the curves showed a local maximum and then decreased gradually. Damage was not observed in this case. This softening was due to self-heating. For high equivalent strain rates, the small shear zone, in which occurred a large degree of deformation, underwent a rapid and localized increase in temperature due to plastic dissipation. Numerical simulation showed [1] that this temperature increase can reach several 100 °C, which explains the large decrease for high equivalent strain rates.

3.1.2. *Semi-hot deformation domain* ($0.3 \leq T/T_f \leq 0.5$)

The phenomenon which dominates in this domain is softening. The slope of the stress–strain curves became negative (see Fig. 15) for all strain rates and for the three steels. The strain rate did not have an influence on the softening but rather on the stress level. This structural softening was not provoked by self-heating but rather by a change in the deformation mechanisms. The dislocation mobility was perturbed by thermally activated phenomena such as dynamic recrystallisation. These phenomena

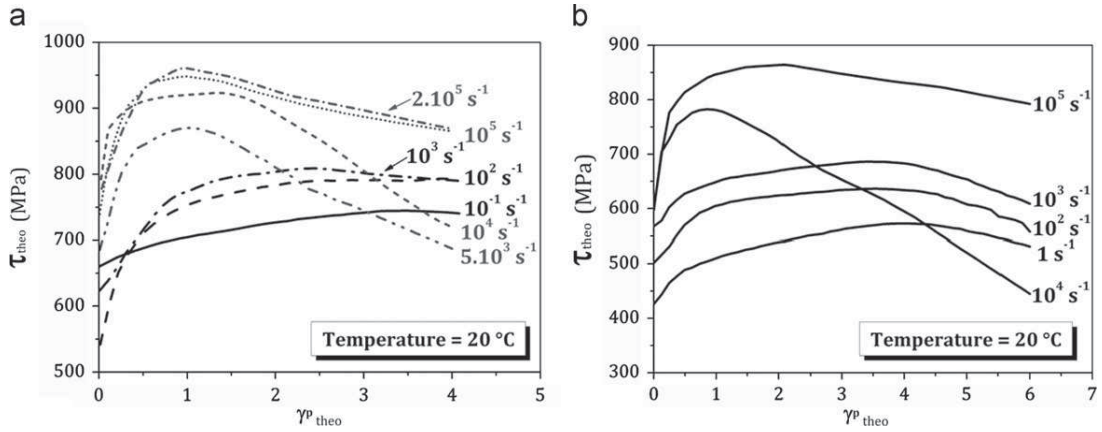

Fig. 14. Evolution of the shear stress as a function of the plastic shear strain at 20 °C for different equivalent strain rates, for steels (a) 42CrMo4-BA and (b) 100Cr6-FP.

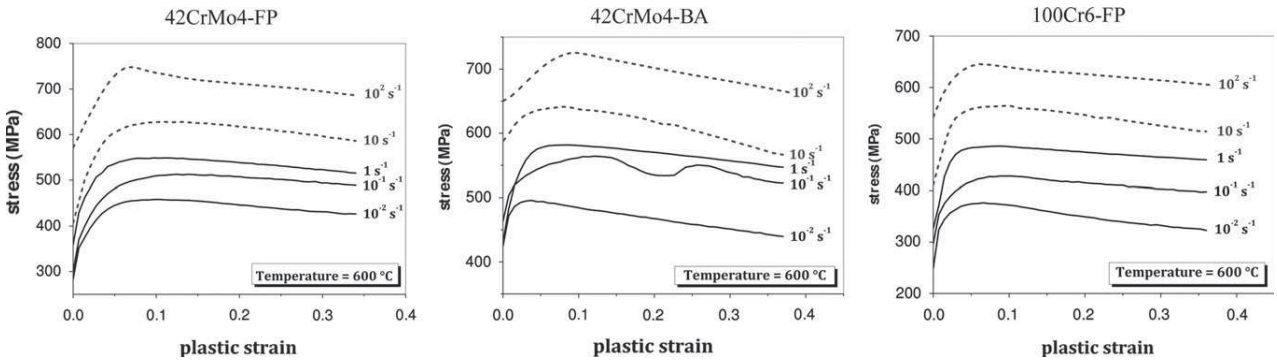

Fig. 15. Evolution of the compressive stress as a function of the plastic strain at 600 °C for different strain rates. Comparison between the three steels studied.

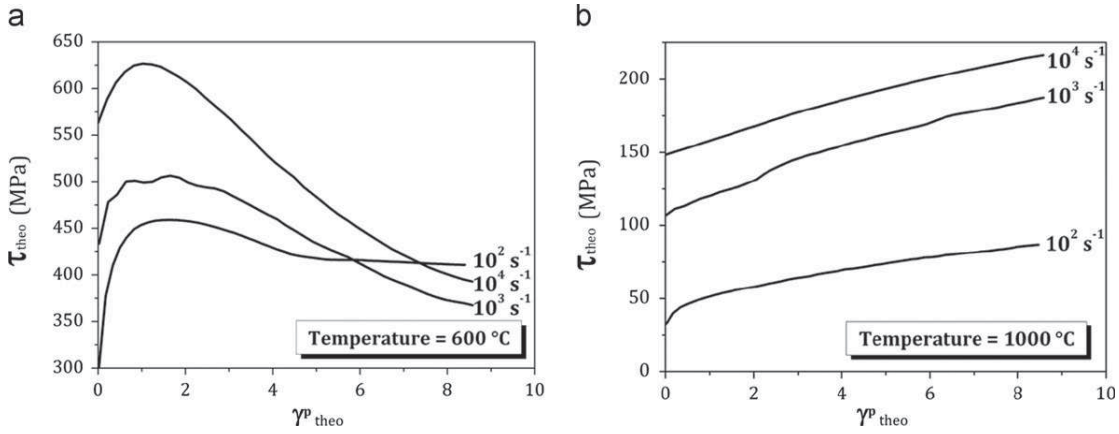

Fig. 16. Evolution of the shear stress as a function of the plastic shear strain at (a) 600 °C and (b) 1000 °C for different equivalent strain rates for the steel 42CrMo4-BA.

appeared even more clearly for the 42CrMO4-BA steel where oscillations in the stress–strain curve were observed (T=600 °C and $\dot{\varepsilon} = 10^{-1}\ s^{-1}$). These oscillations result from an interaction between interstially alloyed elements and dislocations, due to the diffusion of such elements and the pinning of dislocations. Obstacles have a narrow stress field and dislocations may climb. On the opposite, athermal indicates a long range stress field, which may not be overcome by a thermal activated process, no experimental results were obtained that confirm the appearance of this phenomenon in this temperature range. Finally, with respect to the first domain, the flow stress is more sensitive to the strain rate or the material is more viscous.

For the shear tests, for all equivalent strain rates, the shear stress–strain curves are characterised by a local maximum followed by a decrease in the flow stress towards a saturation stress. The rate of this softening, increased with increasing equivalent strain rate. This is a result of the effect of the very localised self-heating in the shear zone of the specimen. The curves in Fig. 16(a) show the limits of the compression tests which only highlighted part of the phenomena accompanying plastic deformation. By limiting these stress–strain curves to a shear strain of 2 (which is equivalent to a strain of 0.5 in compression) it can be seen that the curves are almost identical to those obtained in compression with a local maximum followed by a decrease in the

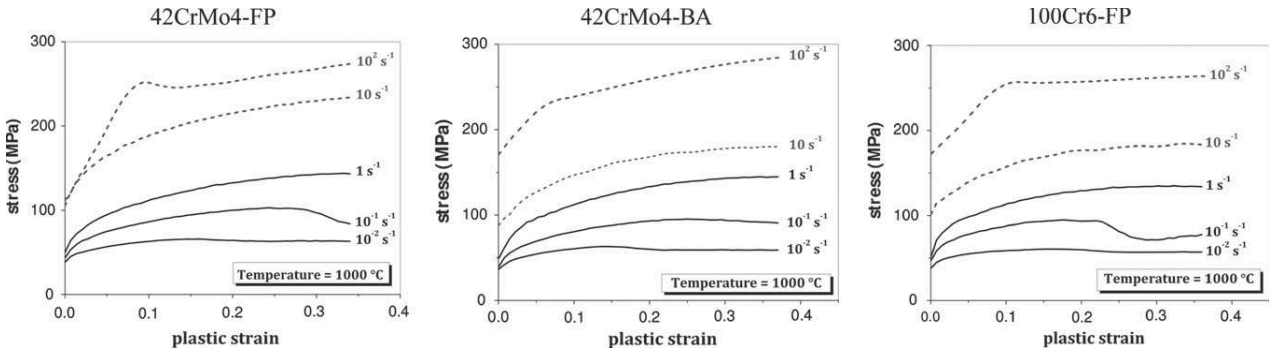

Fig. 17. Evolution of the compressive stress as a function of the plastic strain at 1000 °C for different strain rates. Comparison between the three steels studied.

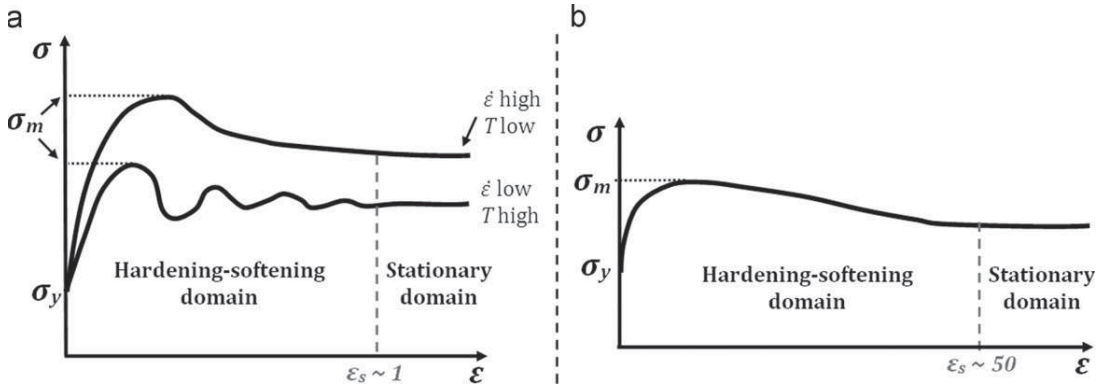

Fig. 18. Characteristic stress–strain curves for a metal with (a) low stacking fault energy and (b) high stacking fault energy [4].

slope which is identical for all strain rates. With these results, it can be concluded that depending on the level of deformation, the equivalent strain rate sensitivity on the flow stress changes, in particular, at saturation, and this sensitivity completely changes sign. Finally, this phenomenon is not observed in compression, not only because the strain and the strain rates are lower, but also because the test is more homogeneous and the self-heating is less intense and less localized.

3.1.3. Hot deformation domain ($T/T_f > 0.5$)

The austenization temperature is between 800 and 900 °C. At these temperatures the material starts to transform from a *body centred cubic* (BCC) structure to a *face centred cubic* (FCC) structure. In this temperature interval, the shape of the stress–strain curves changes completely (see Fig. 17). The stress is more sensitive to the strain rate than in the cold and semi-hot deformation domains. The material behaves in a more viscous manner. Like in the cold domain, the strain rate has an influence on the competition between work hardening and softening. The effect is opposite to the one observed in the first temperature interval. That is, the higher the strain rate, the lower the level of softening and the higher the work hardening. Also, softening that occurs at lower strain rates is different to that observed in the cold and semi-hot deformation domains. The curves drop before achieving a saturation stress at a strain of between 0.3 and 0.4 for the three steel studied. This saturation stress was never achieved in the two other deformation domains.

For the shear tests, the trends are identical to those encountered in compression even for higher strain rates. The equivalent strain rate sensitivity on the stress is limited to a significant increase with strain rate increments. There is no softening phenomena resulting from a local self-heating (Fig. 16(b)). For these temperatures, the flow stress is so low that the power dissipation causing self-heating remains low regardless of the equivalent strain rate and the level of strain.

Montheillet [4] showed that, for materials with low stacking fault energy, it is possible to reach the saturation stress for strains inferior to 1. For the case of materials with high stacking fault energy, the stationary regime is obtained for strains of approximately 50. In this work, it has been confirmed that following austenitization the material behaviour changes from that of a material with high stacking fault energy (Fig. 18(b)) to one with low stacking fault energy (Fig. 18(a)).

To better understand this transition, tests have been done close to the austenitization temperature (see Fig. 19). At 700 and 750 °C, the shape of the curve is similar to the behaviour seen in the semi-hot deformation domain. Continuous softening is observed up until the end of the curve. From 800 °C onwards, softening converges to a saturation state. The change in phase then occurs at a temperature between 750 and 800 °C for the 42CrMo4-FP steel.

Fig. 20 shows thermal expansion curves, for the three steels, measured during heating of the specimens to 1000 °C. A brutal change can be seen, which corresponds to the phase transformation of the microstructure from a BCC crystalline structure to an FCC structure. An FCC structure has greater compacity (0.74) compared to 0.68 for a BCC structure. This different compacity explains the decrease in thermal expansion during phase transformation.

3.2. Processing maps

3.2.1. Efficiency maps

Efficiency maps represent the variation of the efficiency (Eq. (5)) as a function of temperature and strain rate, in the shape

of an iso-efficiency contour plot. The parameter η can also be written as $\eta = J/J_{max}$. The variation of the efficiency η as a function of the thermomechanical conditions therefore represents the evolution of the complementary dissipated power J for this temperature and strain rate range. Several metallurgical mechanisms can contribute to the co-content dissipation during hot deformation. Often, for materials with complex microstructures or for alloys with two phases, the microstructural phenomena that occur simultaneously and/or are interactive. The value of J is the global result of these interactions. The metallurgical phenomena such as dynamic recovery (DRV) and dynamic recrystallization (DRX), internal fracture (i.e. the formation of cavities or the opening of micro-cracks), dissolution or growth of particles or phase, phase transformation or strain-induced precipitation, contributing to the change in power dissipation [9]. In the case of hot forming, the most favorable conditions are those corresponding to the highest values of J (where η is the highest).

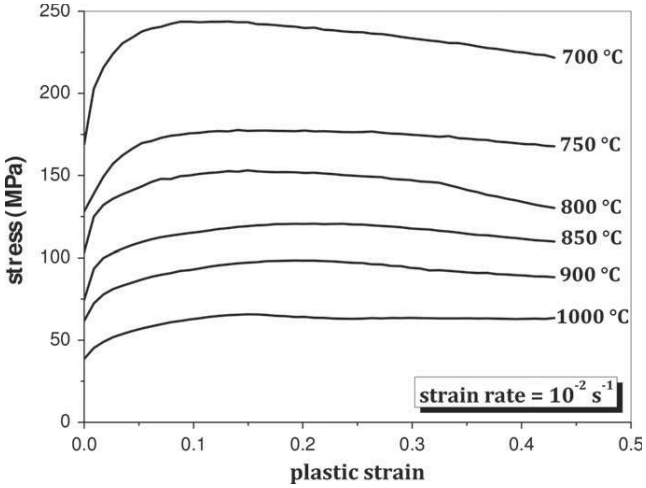

Fig. 19. Evolution of the compressive stress as a function of plastic strain for a constant strain rate of (10^{-2} s^{-1}) and for different temperatures close to the phase change temperature for the 42CrMo4-FP steel.

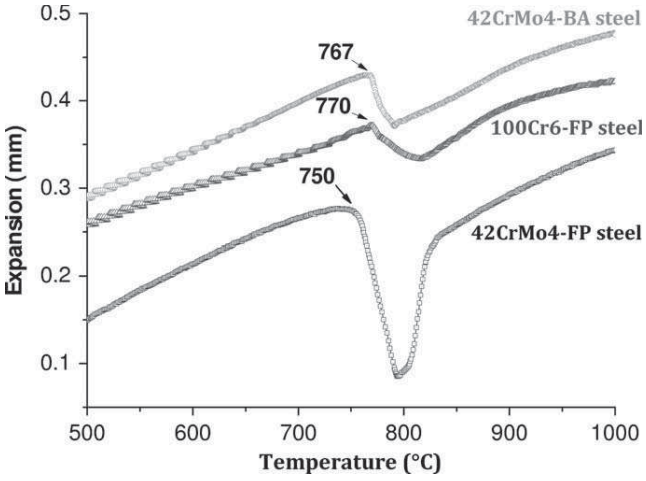

Fig. 20. Evolution of the thermal dilation as a function of the temperature during the heating step.

In the maps shown in Fig. 21, the parameter η is presented in terms of a percentage. For the 42CrMo4-FP steel (see Fig. 21(a)), high values of η (up to (40%) are observed in the temperature range close to the phase change temperature. A slight increase in this parameter is also observed close to a temperature of 400 °C. It is at this temperature that the phenomenon of softening of the flow stress starts. An important variation of this parameter as a function of the strain rate is also detected for a temperature of approximately 1000 °C. This variation can be explained by the phenomenon of recrystallization which is sensitive to the strain rate. For the 42CrMo4-BA steel, the observations are almost the same. An increase in the dissipation power, close to the austenitization temperature is also seen. However, unlike the previous case, no increase in the efficiency η is observed between the temperature range of 200 and 400 °C (see Fig. 21(b)). For the 100Cr6-FP steel the same peaks in dissipation power have also been observed (see Fig. 21(c)).

3.2.2. Instability maps

This map is based on the instability criterion derived from extreme value principles of irreversible thermodynamics applied to large deformation continuum mechanics [10]. As per the first map, the principle of dividing the dissipation power is also applied so that flow instabilities caused by microstructural changes are revealed by this map. The criterion is given by the dimensionless parameter ξ for unstable flow:

$$\xi(\dot{\varepsilon}) = \frac{\partial \ln\left[\frac{m}{(m+1)}\right]}{\partial \ln \dot{\varepsilon}} + m \leqq 0. \tag{7}$$

The temperature and strain rate regimes where ξ is negative implies unstable plastic deformation. Instabilities typically appear in the form of adiabatic shear bands or strain localization in the microstructure. The robustness of this criterion has been largely validated by microstructural observations [8,9]. This approach is often used for temperature ranges and very low strain rates, included in the hot deformation and quasi-static domains. In this work, an attempt is made to apply the complementary power dissipation method over a wide range of thermomechanical conditions.

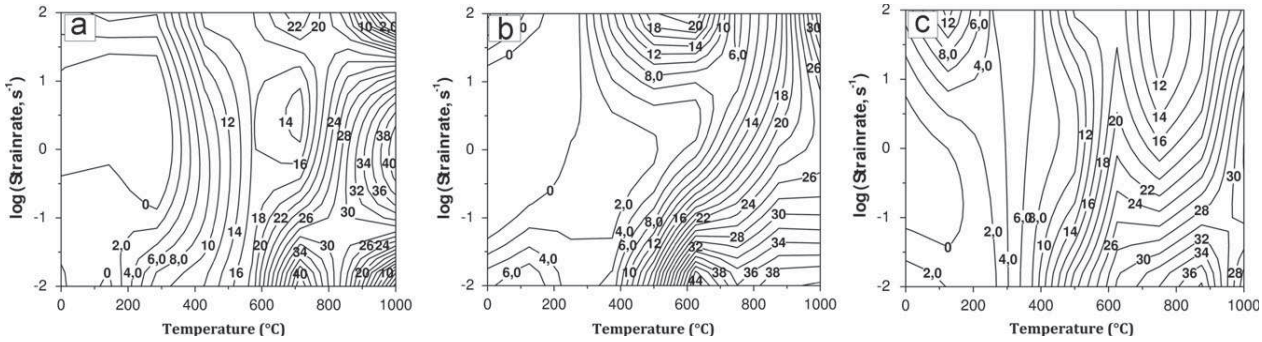

Fig. 21. Efficiency maps (in %) for the three steels studied: (a) 42CrMo4-FP, (b) 42CrMo4-BA and (c) 100Cr6-FP.

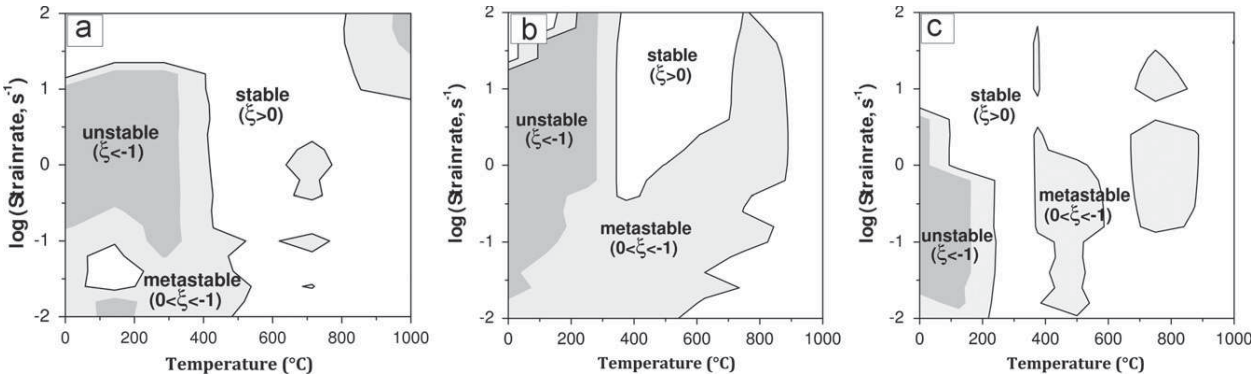

Fig. 22. Unstable flow maps for the three steels investigated: (a) 42CrMo4-FP, (b) 42CrMo4-BA and (c) 100Cr6-FP.

For the 42CrMo4-FP steel, the hot deformation domain is generally stable, regardless of strain rate. Instabilities appear for the cold deformation domain and more precisely between 200 and 400 °C (see Fig. 22(a)). These instabilities could be the source of a flow stress at 400 °C that is higher than the one determined at 200 °C.

Based on Ziegler criterion, two zones, stable and unstable depending on the sign of ξ, must be observed. Chiba et al. [20] justified the existence of a metastable zone observed for values of ξ between -1 and 0 by microstructural observations. This zone is generally between stable and unstable flow. For the 42CrMo4-BA steel, it is observed in cold flow plastic conditions (see Fig. 22(b)). A metastable state is observed for slightly higher temperatures, the metastability being probably caused by stress softening. The deformation of the 100Cr6-FP steel is more stable than the two previous materials. Indeed, the zones of instability and metastability are reduced.

Finally, according to Prasad et al. [9], these instabilities are often observed during cold deformation due to strain localization and the appearance of shear bands. This result confirms previous findings on the influence of increasing strain rates on the microstructure. Indeed, it has been noted that this increase has an effect on the material principally for cold deformation, by the appearance and localization of shear bands due to self-heating and that for hot deformation, it causes only an increase in flow stress.

3.3. Microstructural changes

To extract additional information concerning microstructural changes, metallurgical analyses of the deformed specimens were done. Hardness measurements and SEM observations were conducted at the center of the specimen section after testing. These examinations also help to distinguish the three domains of deformation:

- For cold deformation: hardness remains constant in this domain and is higher than the initial hardness for the three steels (see Fig. 23). This is due to strain hardening. The microstructure does not change.
- For semi-hot deformation: the hardness gradually decreases and above 600 °C it becomes lower than the initial hardness of the material (the ratio of *hardness/initial hardness* is less than 1) except for the 42CrMo4-BA steel. There is more softening than work hardening in this case. This result is confirmed by the stress–strain curves where the flow stress at the end of the deformation is less than the initial yield strength.
- For hot deformation: The austenitization temperature of these steels is between 750 and 800 °C (see Fig. 20). Above this temperature, the material begins to transform from a BCC structure to FCC structure. In this temperature range, the deformed microstructure is not the same, it is partially or completely transformed. This explains the change in shape of the curves. The hardness (normalized by the initial hardness) increases to 2 (see Fig. 23). The material is completely transformed during deformation and the final microstructure, recovered after cooling, is martensite.

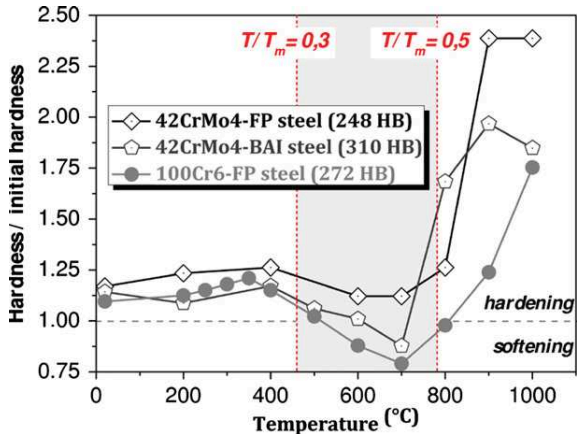

Fig. 23. Hardness of the cylindrical specimens after testing at different temperatures and at a constant strain rate of (10^{-2} s^{-1}) and for a constant strain of 0.6. Comparison between the three steels studied.

Metallurgic observations, of the 42CrMo4-FP steel for example, confirm these findings (see Fig. 24). Indeed, for temperatures below 800 °C, the microstructure is still ferrito-pearlitic and above 800 °C, it is transformed into martensite. It should be noted that the average cooling rate in the Gleeble is between 30 and 50 °C/s. Microscopically, no change in grain size was observed during softening, although a decrease in the hardness of the deformed specimens was often noticed when the curve exhibited softening behaviour.

Finally, a phenomenon is observed for the 42CrMo4-FP and the 100Cr6-FP steels, in which the flow stress in compression or shear at 400 °C is higher than at the temperature of 200 °C. This phenomenon disappears for the bainitic microstructure of the 42CrMo4 steel. In order to observe changes in the shape of the stress–strain curves for intermediate temperatures in this range, a more detailed study was carried out for the 100Cr6-FP steel (see Fig. 25). For temperatures between 20 and 350 °C, the stress increased with temperature. The maximum stress gradually decreased and

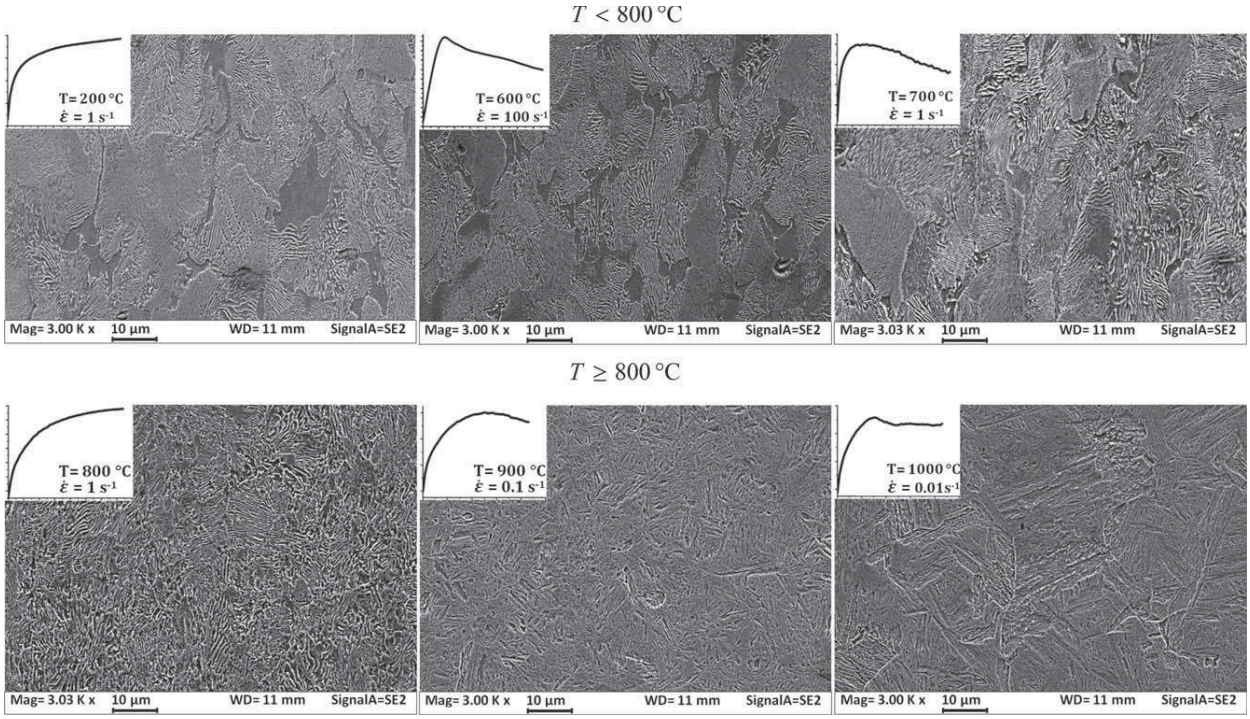

Fig. 24. The microstructure of deformed specimens at different temperatures, at a constant strain rate of (10^{-2} s^{-1}) and for a constant strain of 0.6 for the 42CrMo4-FP steel.

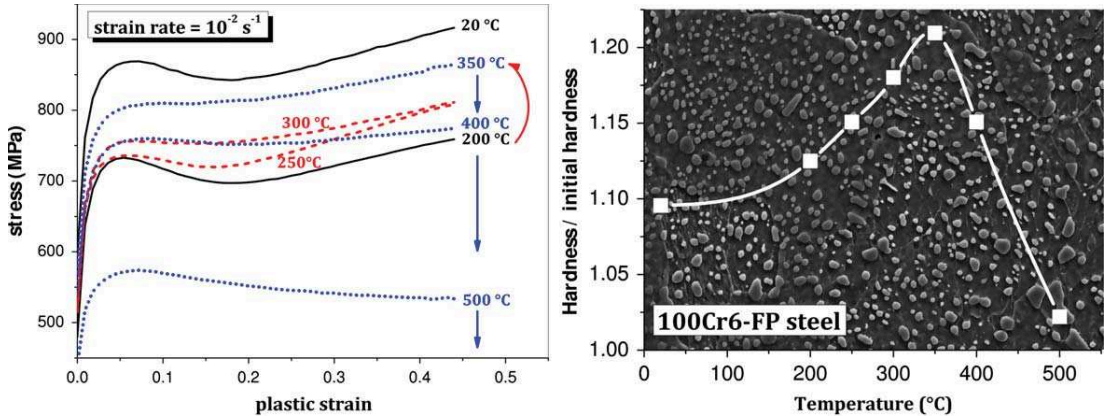

Fig. 25. Behaviour curves for the 100Cr6 steel loaded in compression for a strain rate of $\dot{\varepsilon} = 10^{-2}$ s^{-1} and for temperatures ranging from 20 to 500 °C and the hardness of the deformed specimens.

the characteristic "bump" shape of the stress–strain curve for this steel progressively disappeared. The hardening that follows this local maximum was also slightly increased. From a temperature of T=350 °C, the local stress maximum disappeared, the hardening rate decreased and the evolution of stress with temperature decreased with increasing temperatures. This study was complemented by microscopic observations and an analysis of the hardness (see Fig. 25). The microstructure does not exhibit significant changes: carbides have same size. For temperatures up to 350 °C, the hardness increased and then decreased, which validates the findings concerning work hardening.

This phenomenon may be identical to instabilities encountered in the literature [21,22]. For the phenomenon of ageing dynamics, this inversion of the sensitivity of the stress as a function of temperature can be observed. This phenomenon usually appears in the ferritic phase of steels alloyed with manganese for temperatures between 20 and 400 °C. It corresponds to the formation of manganese carbides and nitrides following the association of carbon and nitrogen atoms, which are in solid solution in the ferrite, with manganese atoms. This transformation can be enhanced by plastic deformation and is very sensitive to the deformation temperature. Wagner et al. [23] showed that a ferrito-pearlitic steel A48 (with 0.769% Mn, 0.198% C and 0.0083% N) has a higher tensile yield stress at 200 and 300 °C compared to 20 °C. These phenomena occur at the atomic scale and require special means of observations such as a TEM to observe the precipitates formed during deformation and internal friction tests (mechanical spectroscopy) to quantify the distribution of the atoms in solid solution [23]. For these reasons, very few microscopic investigations of ageing dynamics have been undertaken. Finally, the inversion of the strain rate sensitivity on the stress for the same steel but with a different microstructure (bainite) confirms that the phenomenon explaining this inversion is ageing dynamics and appears only in the ferritic phase.

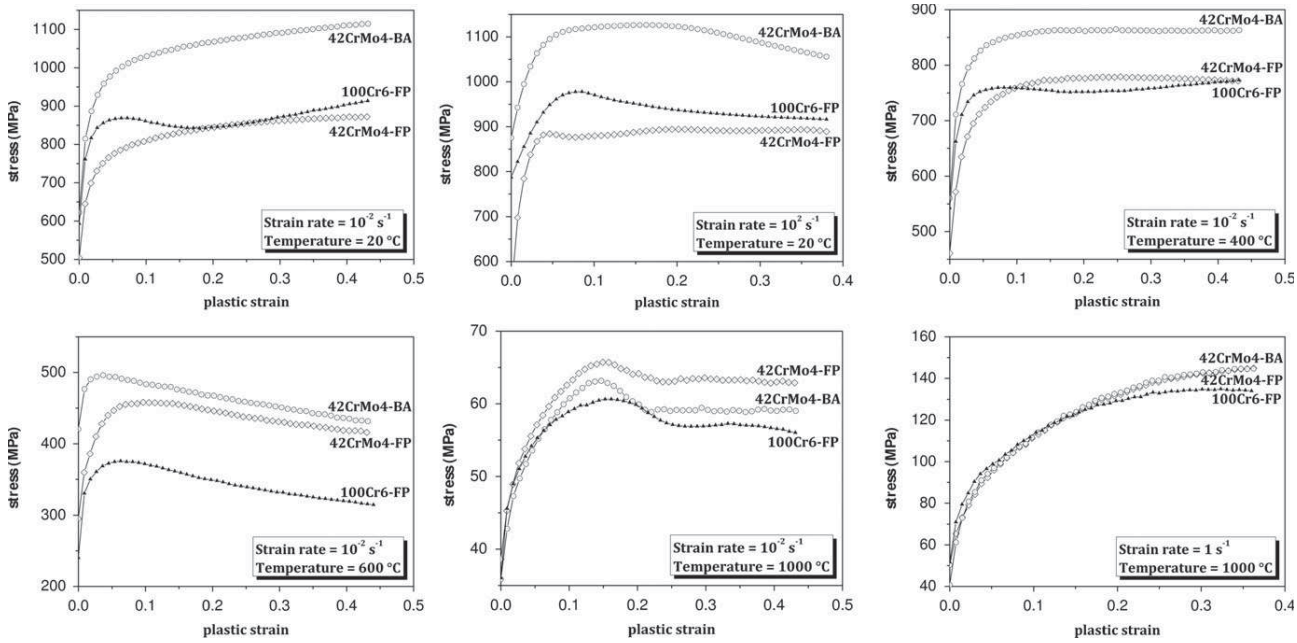

Fig. 26. Comparison of the shape of the stress–plastic strain curves for three steels studied in the three deformation domains.

4. Discussion

This investigation of the deformation behaviour of three steels over a large range of strain rates and temperatures, for two loading conditions (i.e. compression and shear), has highlighted the existence of three deformation domains (cold, semi-hot and hot deformation) that can be defined by certain temperature ranges. The shape of the stress–strain curves and the evolution of the flow stress as a function of the temperature are very different in each domain. Along with the influence on the flow stress, the strain rate plays a role on phenomena accompanying plastic deformation such as work hardening and softening. Comparison between the three steels shows much similarity in terms of thermomechanical behaviour (see Fig. 26). Indeed, despite their compositional and microstructural variations, temperature and strain rate sensitivity is almost identical. The observed phenomena in each deformation domains are very similar, which is encouraging from a modelling point of view. The development of a global constitutive law that can be identified over such a large range of rheological parameters appears to be possible. However, small differences have also been observed in terms of the shape of the stress–strain curves at low temperature and low strain rate, especially for the 100Cr6 steel, where local maximum appears at the start of the plastic domain, followed by an increase in the flow stress. The globular microstructure is perhaps the origin of this local maximum that subsequently disappears when temperature is increased.

Finally, this rich experimental database offers the possibility to propose and adjust more sophisticated constitutive models that can account for certain phenomena essential to the improvement of numerical simulations of manufacturing processes. Indeed, Calamaz et al. [3] showed that the inclusion of thermal softening in a modified Johnson–Cook model [17] results in a more accurate chip form for the simulation of the machining of TA6V for different cutting conditions. Lurdos [7] modified the Voce law [24] in order to propose a more general thermo-visco-plastic model that takes into account certain phenomena observed over a wide range of rheological parameters such as the local maximum observed for dynamic tests on a 316L stainless steel. These studies and the experimental work conducted here show that the three main phenomena observed (the effect of the temperature, the effect of the strain rate and strain hardening–softening) cannot be decoupled. Strong coupling in the modeling of these effects is therefore necessary. Multiplicative constitutive equations such as the Johnson–Cook model, which does not include coupling, cannot be applied to manufacturing processes such as machining where the material is subject to a very wide range of temperatures and strain rates. A comparison between the different classes of constitutive models: empirical models (coupled and uncoupled), semi-empirical models and physical models, applied to the numerical simulation of orthogonal cutting and to plane strain tests is presented in [12].

In summary, the dissipation and instability maps show that the three steels investigated can be used for hot forming processes. This is the domain in which their power dissipation is a maximum and they have greatest stability, especially for the 100Cr6-FP steel where the stability zone is large, which confirms the good forgeability of this steel for the manufacturing of bearings. The approach based on the complementary power dissipation is often used to characterize the dynamic behaviour during deformation process. Despite the thermodynamic considerations, this approach is phenomenological. The processing maps do not fully estimate the microstructural changes. Montheillet et al. [25] have discussed the short-comings of this approach. They showed that these maps do not enable estimation of the conditions for dynamic recrystallization. In terms of the present investigation, even though the saturation stress was not used, the dissipation and instability maps can highlight certain phenomena but no definitive conclusions can be made about their existence. Alone they are insufficient to establish favourable conditions for deformation. Additional information must be provided by microstructural observations. The determination of these maps also requires the implementation of several tests at different temperatures and very low strain rates. Interpolation is often used to complete the required database. This can lead to undetection of a number of phenomena occurring at specific temperatures or strain rates. In terms of the present study, despite the extensive database with broad range of rheological parameters,

interpolation using Bezier polynomials was necessary to determine the maps.

One of the major problems of studies concerning rheology in machining and forging is the lack of experimental data. This penalizes numerical analysts who use phenomenological and very simple models (such as the Johnson–Cook model [17]) [26], the identification of which requires only a few tests [5,27] and that have a limited range of validity, which is more restrictive than the range of the rheological parameters observed in machining or forging operations. Also, it is possible to find in the literature different values of the same model parameters for identical materials [28,29]. Contradictions in the experimental results can also be found depending on the different experimental devices used to cover a wide range of rheological parameters.

5. Conclusion

In this work, an experimental study of the rheology of two major families of steels with different microstructures was conducted over a wide range of temperatures and strain rates, characteristic of forging and machining forming processes. Three deformation domains have been distinguished depending on the behaviour and the changes in microstructure (both hardness and phase changes). Following this study, each domain was characterized by its thermomechanical behaviour (i.e. the competition between hardening and softening, the strain rate sensitivity on the stress, softening (recrystallization or recovery), etc.). Finally, based on thermodynamical considerations, the conditions of thermomechanical instabilities and microstructural changes are highlighted by mapping the distribution of dissipated power.

To conclude, it is hoped that this comprehensive investigation of the rheology of steels over a wide range of deformation, temperature and strain rate will allow the development of more elaborate constitutive laws that take into account certain phenomena active in forming processes such as machining and forging. This will subsequently improve the numerical simulation of such process by introducing more precise stress–strain constitutive equations, in which the model parameters can be identified in a deterministic manner.

References

[1] Changeux B, Lebrun J-L. Microstructural modifications and material response in machining of steels. J Phys IV 2001;11:4213–20.
[2] MSaoubi R, Lebrun J-L, Changeux B. A new method for cutting tool temperature measurement using ccd infrared technique: influence of tool and coating. Mach Sci Technol 1998;2:369–82.
[3] Calamaz M, Coupard D, Girot F. A new material model for 2d numerical simulation of serrated chip formation when machining titanium alloy ta6v. Int J Mach Tools Manuf 2008;48:275–88.
[4] Montheillet F. Métallurgie en mise en forme. Tech l'ingé 1996;1M600:1–20.
[5] Tounsi N, Vincenti J, Otho A, Elbestawi M. From the basic mechanics of orthogonal metal cutting toward the identification of the constitutive equation. Int J Mach Tools Manuf 2002;42:1373–83.
[6] Mulyadi M, Rist MA, Edwards L, Brooks JW. Parameter optimisation in constitutive equations for hot forging. Mater Process Technol 2006;117:311–4.
[7] Lurdos O. Loi de comportement et recristallisation dynamique: approches empirique et physique. PhD thesis. Ecole Nationale Supérieure des Mines de Saint-Etienne; 2008.
[8] Prasad Y. Processing maps: a status report. J Mater Eng Perform 2003;12:638–45.
[9] Prasad Y, Gegel H, Doraivelu S, Malas J, Morgan J, Lark K, et al. Modeling of dynamic material behavior in hot deformation: forging of ti-6242. Metall Trans A 1984;15:1883–92.
[10] Ziegler H. Some extremum principles in irreversible thermodynamics with applications to continuum mechanics. Progr Solid Mech 1965;4:91–193.
[11] Prager W. Viscoplasticity and locking solids. Trans Soc Rheol 1957;1:169–75.
[12] Hor A. Simulation physique des conditions thermomécaniques de forgeage et d'usinage-caractérisation et modélisation de la rhéologie et de l'endommagement. PhD thesis. Arts et Métiers ParisTech; 2011.
[13] Committee AIH. ASM Handbook: properties and selection: nonferrous alloys and special-purpose materials, vol. 2, 10th ed. ASM International; 1990.
[14] Longère P, Dragon A. Adiabatic heat evaluation for dynamic plastic localization. J Theor Appl Mech 2007;45:203–23.
[15] Meyers M, Subhash G, Kad B, Prasard L. Evolution of microstructure and shear-band formation in alpha-hcp titanium. Mech Mater 1994;17:175–93.
[16] Habak M, Lebrun J-L, Morel A. A study of the influence of the metallurgical state on shear band and white layer generation in 100Cr6 steel: application to machining. In: Proceedings of the 10th ESAFORM conference; 2007. p. 691–6.
[17] Johnson G, Cook W. A constitutive model and data for metals subjected to large strains, high strain rates and high temperatures. In: Proceedings of the 7th international symposium on ballistics, The Hague, Netherlands; 1983.
[18] El-Magd E, Abouridouane M. Characterization, modelling and simulation of deformation and fracture behaviour of the light-weight wrought alloys under high strain rate loading. Int J Impact Eng 2006;32:741–58.
[19] Meyer L, Herzig N, Halle T, Hahn F, Krueger L, Staudhammer K. A basic approach for strain rate dependent energy conversion including heat transfer effects: an experimental and numerical study. J Mater Process Technol 2007;182:319–26.
[20] Chiba A, Lee S-H, Matsumoto H, Nakamura M. Construction of processing map for biomedical Co–28Cr–6Mo–0.16N alloy by studying its hot deformation behavior using compression tests. Mater Sci Eng A 2009;513–514:286–93.
[21] Ranc N, Wagner D. Some aspects of portevin-le chatelier plastic instabilities investigated by infrared pyrometry. Mater Sci Eng A 2005;394:87–95.
[22] Ranc N, Wagner D. Experimental study by pyrometry of portevin-le chatelier plastic instabilities—type a to type b transition. Mater Sci Eng A 2008;474:188–96.
[23] Wagner D, Roubier N, Prioul C. Measurement of sensitivity to dynamic strain aging in C-Mn steels by internal friction experiments. Mater Sci Technol 2006;22:301–7.
[24] Voce E. The relationship between stress and strain for homogeneous deformation. J Inst Met 1948;74:537–62.
[25] Montheillet F, Jonas J, Neale K. Modeling of dynamic material behavior: a critical evaluation of the dissipator power co-content approach. Metall Mater Trans A 1996;27:232–5.
[26] Barge M, Hamdi H, Rech J, Bergheau J-M. Numerical modelling of orthogonal cutting: influence of numerical parameters. J Mater Process Technol 2005;164-165:1148–53.
[27] Zemzemi F, Rech J, Salem WB, Dogui A, Kapsa P. Identification of a friction model at tool/chip/workpiece interfaces in dry machining of AISI4142 treated steels. J Mater Process Technol 2009;209:3978–90.
[28] Huang Y, Liang S. Force modelling in shallow cuts with large negative rake angle and large nose radius tools—application to hard turning. Int J Adv Manuf Technol 2003;22:626–32.
[29] Guo Y, Wen Q, Woodbury K. Dynamic material behavior modeling using internal state variable plasticity and its application in hard machining simulations. J Manuf Sci Eng, Trans ASME 2006;128:749–59.